Mechanical Property Heterogeneity in Additively Manufactured Nickel Superalloy

A.N. Forsey, Y.B. Das, T.H. Simm, D. Clarke, J. Boswell, S. Gungor, R.J. Moat

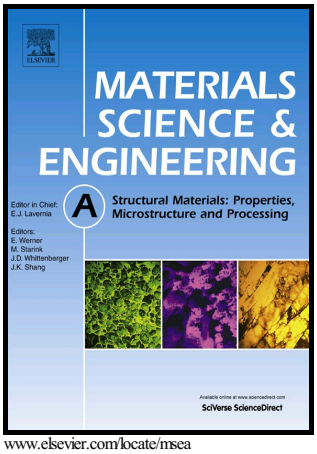

www.elsevier.com/locate/msea

PII: S0921-5093(17)31624-6
DOI: https://doi.org/10.1016/j.msea.2017.12.025
Reference: MSA35867

To appear in: *Materials Science & Engineering A*

Received date: 28 September 2017
Revised date: 7 December 2017
Accepted date: 8 December 2017

Cite this article as: A.N. Forsey, Y.B. Das, T.H. Simm, D. Clarke, J. Boswell, S. Gungor and R.J. Moat, Mechanical Property Heterogeneity in Additively Manufactured Nickel Superalloy, *Materials Science & Engineering A,* https://doi.org/10.1016/j.msea.2017.12.025

Mechanical Property Heterogeneity in Additively Manufactured Nickel Superalloy

A.N. Forsey[1], Y.B. Das[1], T.H. Simm[2], D. Clarke[3], J. Boswell[3], S. Gungor[1], R.J. Moat[1]

[1]Open University, MK7 6AA, UK;

[2]Swansea University, SA1 8EN, UK;

[3]Rolls Royce Plc, DE24 8BJ, UK

Metallic additive manufacturing (AM) techniques do not produce a homogenous structure. Digital image correlation is used to quantify significant variations in mechanical properties in an AM nickel superalloy. Non-uniform properties at multiple length-scales are demonstrated, which could explain the poor mechanical properties common with AM alloys.

Extensive investigation over the last 10 years has shown that laser-based AM of nickel superalloys exhibit non-optimal microstructures and hence mechanical properties. High crystallographic texture[1–3], columnar grain structure[4–6] and intergranular defects[7] are common due to epitaxial growth. The alloy's use is also limited by high residual stresses[8,9] suboptimal aging[10] and anisotropic mechanical properties[11–15]. Efforts are being made to mitigate these problems with varied levels of success. Notably, the alloy CM247 has shown promise in controlling the microstructures formed during AM[5,13]. Hence this alloy was used in the following work, however other Nickel base alloys have shown similar scope [11,16].

Two tensile specimens were EDM machined from a sheet of nickel superalloy CM247[4] manufactured using selective laser melting. Test piece dimensions were based on ASTM E8M (Figure 1a and b) and orientated with the loading axis perpendicular to the z-axis (the direction of build). Two different samples were measured to provide information about strain at different length scales, and are referred to meso-scale and micro-scale throughout. The tensile specimens were ground for equal times on both front and back faces, to remove surface roughness, and polished to a mirror finish. Final polishing was performed using an oxide suspension (OPS) to eliminate plastic damage from the surface. Optical microscopy and electron backscatter diffraction (EBSD) were used to characterise the microstructure of the specimen surface (Figure 2a and b). The microstructure observed with optical microscopy, although not equiaxed shows a significantly less directional microstructure compared to that seen with EBSD. Furthermore, EBSD reveals bundles of grains with very similar grain orientation. The colour scale in Figure 2b shows misorientation from a {001} orientation, and it is clear that this is the most prevalent growth orientation, as would be expected from epitaxial growth in face-centred cubic nickel.

The meso-scale sample (Figure 1a) was pulled at a strain rate of 0.01 s^{-1} at room temperature and 850 images were taken at 1 Hz using a Nikon DS-Qi2 monochrome camera. The optics used were a Nikkor 200 mm f4 IF ED micro lens spaced by macro bellows, producing an image with a pixel size of 2.6 µm. A 30 second exposure to Kalling's reagent produced a surface speckle pattern suitable for digital image correlation (DIC) on the polished surface. DIC is a computational technique that tracks the movement of small regions of a surface. The displacements of small

subregions of the images are obtained by pattern tracking between displacement steps[18]. This produces a regular grid of displacement vectors from the sample surface for each load step and consequently maps of 2D surface strains. Images were taken during deformation and displacements were obtained using the commercial DIC package DaVis 8.3[17], using a least squares based algorithm[18]. A subregion size of 31 x 31 pixels with a 10 pixel step size. The 2D plots (Figure 3b and c) were obtained using a sliding bilinear least square fit to differentiate the displacement field, using a differentiation length of 159 µm.

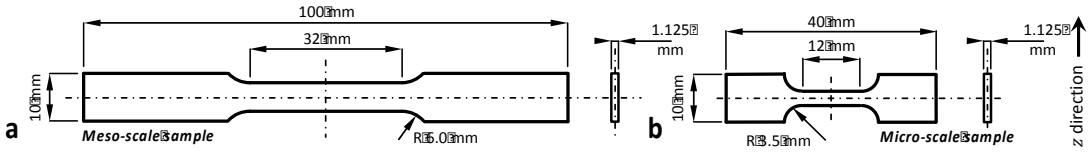

Figure 1: a) Meso-scale sample design, b) Micro-scale sample design

For mechanical property calculation, a separate high density DIC analysis was performed. This analysis had a subregion size of 21 x 21 pixels and a stepsize of 1 pixel, and was used to maximise the amount of data contained within each averaging stripe. The elastic region is calculated for each stripe by minimising the difference between the tangent and secant moduli, with tangent modulus used as the reported value. The intersection of this modulus, offset by 0.002, with a cubic spline fit to the raw data, is used to calculate the proof stress. The error bars in Figure 3d and e are calculated by splitting the DIC data into four separate datasets and performing the same calculation process on these distinct vector maps.

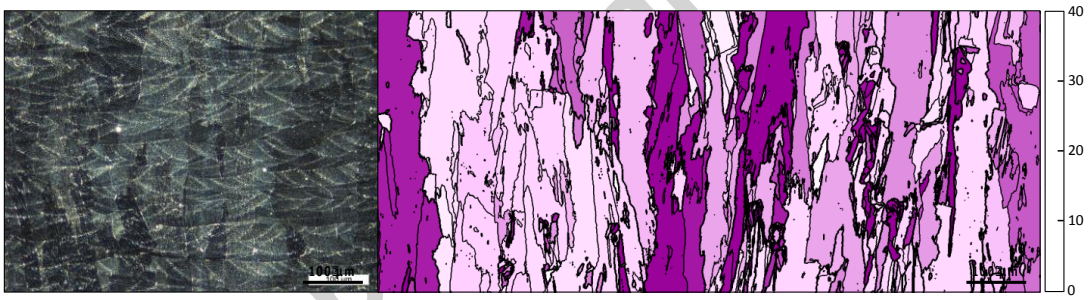

Figure 2: a) Optical micrograph b) EBSD showing the difference from the {001} orientation and an overlay of micro-scale test site.

When loaded perpendicular to the z-axis (see Figure 1a and b), grains close to a {001} orientation (white in Figure 2b) have a theoretical stiffness of ~170 GPa[19] while those with an orientation close to {011} could have a stiffness as high as 200 GPa (Data reported by Dye et al.[19], used for comparison purposes here is for the Nickel superalloy, Waspaloy, however orientation dependence of different superalloys is not expected to vary significantly). In a similar manner, plastic flow is also orientation dependent, with different slip systems and hence strain expected in different orientations. Hence, clusters of grains with similar orientations are not expected to behave the same as a typical polycrystal. This potentially large anisotropy has significant implications for structural integrity and component life prediction, as stress localisation inevitably leads to plastic deformation mismatch.

To investigate the influence of this microstructure, in situ tensile tests were conducted in combination with DIC. The image magnifications were optimised for the length scales of microstructural variation observed in these samples. The preparation

required a gold remodelled surface to be produced on the sample to function as a speckle pattern for DIC[20,21]. Images were taken using a Zeiss Supra 55VP field emission gun scanning electron microscope (FEG SEM) using backscatter electron mode, an accelerating voltage of 20 kV and a working distance of 16 mm, with a pixel size of 91 nm. The strain was applied by a 4.5 kN ADMET mini-tensile testing machine in situ, at a strain rate of 0.01 s^{-1}. The loading was halted during imaging so that three images could be acquired and averaged at each load step. The images were analysed using a DIC subregion of 11 x 11 pixels and a step size of 5 pixels and the strain is plotted using a differentiation length of 3.3 μm.

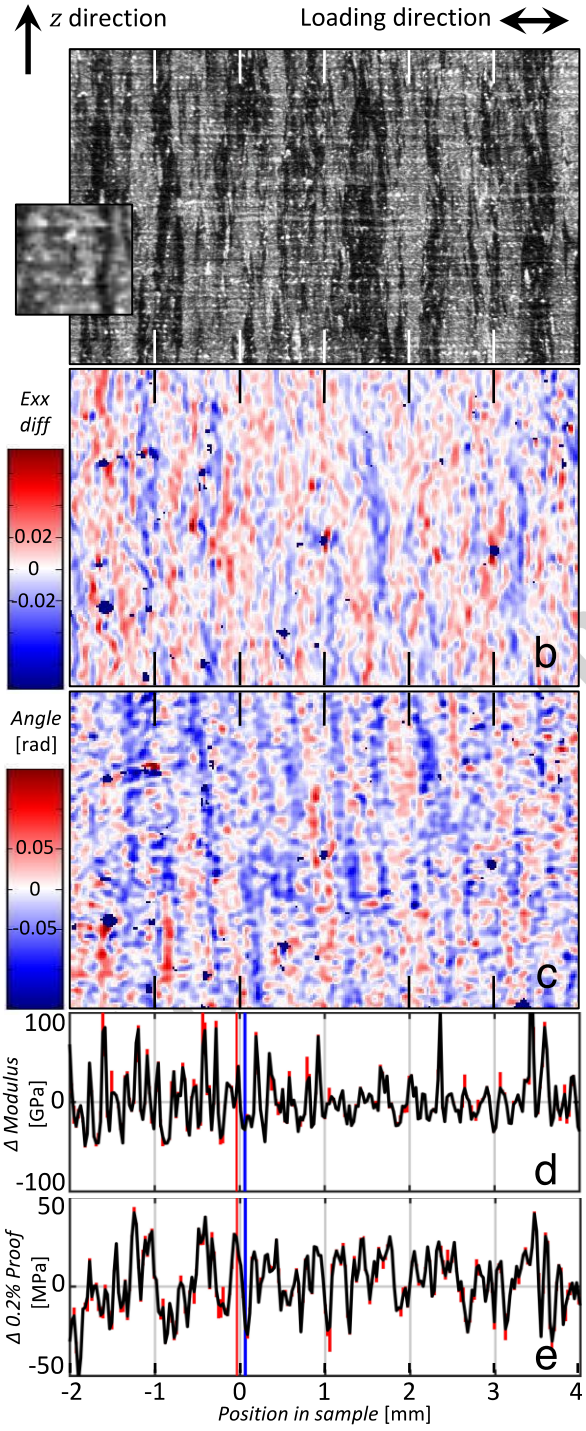

Figure 3: Meso-scale DIC results, a) an example image used for analysis with insert showing pixel definition, b) spatially resolved map of loading direction strain (Exx) difference to global value at 0.075 strain, c) spatially resolved map of principal strain angle with respect to the loading direction at the same strain value, d) variation of elastic modulus along the length of sample gauge and e) variation of 0.2% proof stress along the length of sample gauge. Red and blue vertical lines in d and e correspond to locations of data extraction for Figure 5. Red bars on parts d and e indicate the measured systematic error of the property extraction process.

For a global strain of 0.075, Figure 3b and c show spatially resolved maps of the correlations made from meso-scale images; the reference image is shown in Figure 3a. In Figure 3b, a banded strain response is observed with a range of approximately 0.1 strain, and a periodicity of ~400 μm. Similarly, Figure 3c has a banded pattern perpendicular to the loading direction with a similar periodicity. This figure shows the range in principal strain angle with respect to the loading direction. The range in angle is 0.3 radians, which is an unexpected range for a uniaxial tensile test.

From Figure 2b, the vertical regions of epitaxial growth can be seen, which should lead to relatively consistent material properties in the *y* direction. This was the key assumption to enable the calculation of material properties from the DIC maps, by averaging the strain across the width of the test specimen (*y* direction). The strain was calculated by fitting a bilinear polynomial to stripes of the image perpendicular to the loading direction, using the optical flow approach[22]. By taking stripes across the full width of the sample (*y* direction), a constant stress assumption can be made for each region. This enables stress versus strain plots to be made for each stripe and these are then interrogated to obtain the elastic modulus and proof stress. For this study, the constant stress assumption is only approximate and a number of the stripes will cross material property boundaries and in others local constraint effects will alter the stress state. In both cases this is likely to result in an underestimate of the variation in material properties along the sample.

Figure 3d and e show line plots calculated from rectangular, 65 μm in *x* and 4000 μm in *y*, striped regions calculated from a separate high density DIC analysis. Figure 3d shows the elastic modulus, and Figure 3e the 0.2% proof stress extracted from the stress-strain curves produced from the rectangular stripe strain calculation. Both are observed to have a similar periodicity to that found in the 2 dimensional plots. A range of ~75 GPa in elastic modulus and ~60 MPa in proof stress offer extreme uncertainties compared to the values calculated from global strain measurements. These values are likely to be underestimates because the procedure averages out extremes of behaviour.

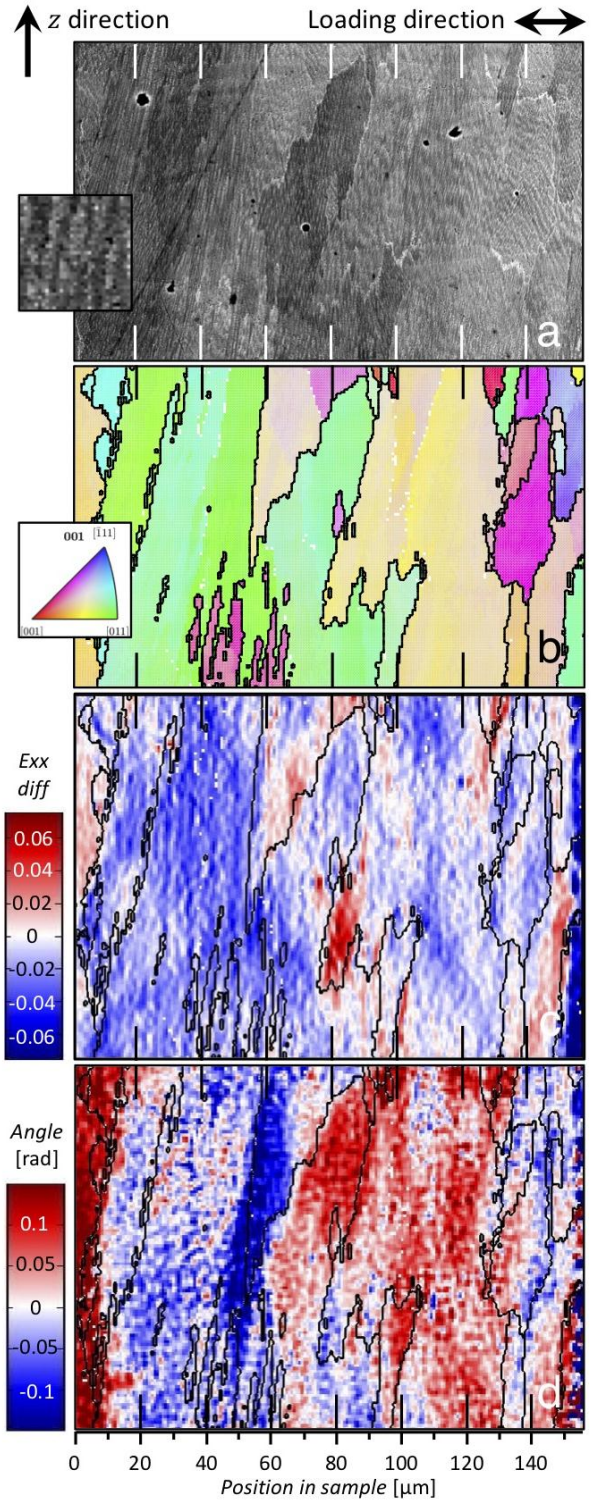

Figure 4: Micro-scale DIC results, a) an example image used for analysis with insert showing pixel definition, b) Inverse pole figure EBSD orientation map of area tested using DIC c) spatially resolved map of difference in loading direction strain (Exx) to sample average (of 0.075 strain) and d) spatially resolved map of principal strain angle with respect to the loading direction.

To link the mesoscopic deformation to microstructural features, a similar second test was performed using SEM imaging. This enabled electron backscatter diffraction (EBSD) to be performed on the same area prior to straining; this region is marked in

Figure 2b. Figure 4a shows an SEM image of the micro-scale sample with a gold remodelled surface and Figure 4b shows the EBSD IPF map of the area imaged prior to straining. Figure 4c and d show *Exx* and the principal strain angle relative to the loading direction respectively. Figure 4 is plotted at the same global strain value as Figure 3 to enable direct comparison between the length scales. In the meso-scale test (Figure 3), a similar range in strain and principal strain offset angle are observed. However, the sudden changes in both strain and principal strain angles seen at grain boundaries can only be resolved at the higher magnification. Conversely, at this higher magnification it is impossible to compare the scale and periodicity of these features. However, the spread in measured values at both length scales is precisely comparable. It is clear to see that the variation in strain accommodation seen in Figure 3b is radically smoothed by the resolution of the camera. At the scale seen in Figure 4c, the 400 μm frequency periodicity of strain localisation is revealed, as discontinuous regions of significant deformation. The interfaces of these regions are between grains close to a {011} orientation and those closer to {001} (Figure 4b), confirming the cause of the variation to be crystallographic.

Variations in elastic modulus and proof stress of the order observed here pose significant issues for component performance and life predictions. Invariably a single value for proof stress and elastic modulus are used for such calculations. In special cases one might consider using anisotropic mechanical properties, such as single crystal turbine blades and highly texture weld metal, but spatially resolved variations in anisotropy would be unprecedented. This is more the reserve of the microstructural modelling community and not the structural integrity or lifing community.

The extent of the considerations that must be made are illustrated in Figure 5, with part a showing the global tensile stress-strain curve for this sample. A proof stress of 818 MPa and an elastic modulus of 169 GPa is comparable to properties reported by Geiger[16] and more than adequate for as deposited SLM materials. Figure 5b shows two tensile curves taken from neighbouring locations indicated in Figure 3d and e (19 μm apart). One is located in a low strain (red) and one from a high strain (blue) region and plotted alongside the global stress strain curve. The difference in elastic modulus is plainly obvious, but similarly, the proof stress between the 3 curves varies by 50 MPa. This effect is further exacerbated by the proposition from Figure 4, that these steps in material properties are discontinuous; this implies extreme states of local constraint for the weaker sections of the material. Such localisations in deformation will result in regions prone to cracking and premature failure, when compared to macroscopic stress-strain data. Furthermore, as a result of this crystallographic heterogeneity, usual post processing techniques, such as heat treatment or HIPing (hot isostatic pressing), will have little influence[13,23].

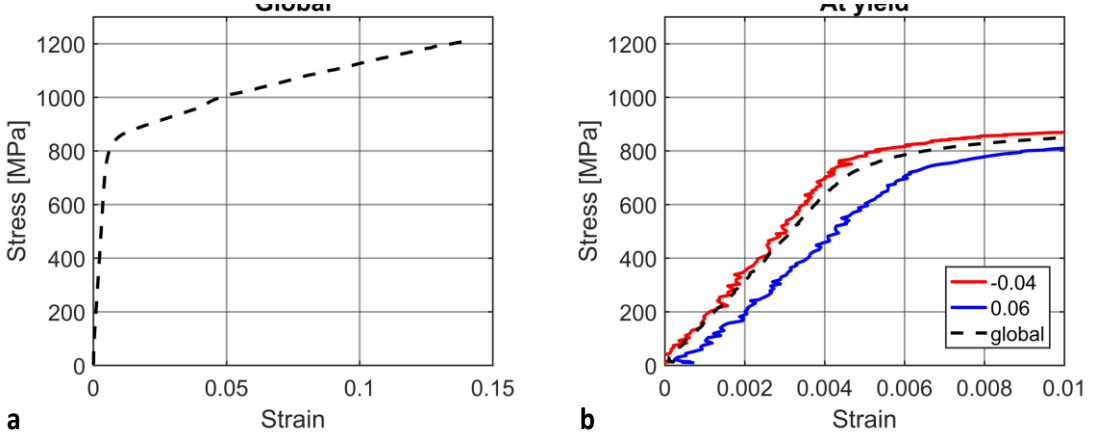

Figure 5: (a) full tensile curve and (b) tensile curve to 0.01 strain of meso-scale sample, with curves from the red and blue regions highlighted in Figure 3 superimposed, showing the difference in both modulus and proof stress seen in Figure 3d and e respectively.

Digital image correlation has been used to measure the variations in mechanical properties in SLM nickel superalloys. Whether considering the tensile curves plotted in Figure 5 or the strain maps shown in Figures 3 and 4, the heterogeneity in mechanical properties are clear. Grain-to-grain variations in mechanical properties, such as those presented in Figure 4 are traditionally only of interest of material scientists because they become aggregated over large volumes. The results presented in this manuscript do not appear to show the same aggregation, with variations in mechanical properties appearing to be related to the crystallographic heterogeneity inherent to AM materials. The current inability to crystallographically randomise additively manufactured metallic structures is a current obstacle in the AM revolution; not just for complex material systems, but also for relatively mundane applications. The techniques and results presented in this manuscript offer a mechanism to measure, and therefore account for, these variations in mechanical properties. While continued efforts are being made to control microstructures in AM materials, measurements such as these could be used as a way of improving reliability of structural integrity and lifing models.

The authors would like to thank Rolls-Royce plc for their technical and financial support during this research project as part of the SAMULET 2 program. T. H. Simm acknowledges support from the European Regional Development Fund via the Ser Cymru II fellowship program.

[1] R.J. Moat, a. J. Pinkerton, L. Li, P.J. Withers, M. Preuss, Crystallographic texture and microstructure of pulsed diode laser-deposited Waspaloy, Acta Mater. 57 (2009) 1220–1229. doi:10.1016/j.actamat.2008.11.004.

[2] T. Bauer, K. Dawson, A.B. Spierings, K. Wegener, Microstructure and mechanical characterisation of SLM processed Haynes® 230, J. Chem. Inf. Model. 53 (2013) 1689–1699. doi:10.1017/CBO9781107415324.004.

[3] L.L. Parimi, R.G. A., D. Clark, M.M. Attallah, Microstructural and texture development in direct laser fabricated IN718, Mater. Charact. 89 (2014) 102–111. doi:10.1016/j.matchar.2013.12.012.

[4] L.N. Carter, M.M. Attallah, R.C. Reed, Laser Powder Bed Fabrication of Nickel-Base Superalloys: Influence of Parameters; Characterisation, Quantification and Mitigation of Cracking, in: Superalloys 2012, 2012: pp. 577–586. doi:10.1002/9781118516430.ch64.

[5] L.N. Carter, C. Martin, P.J. Withers, M.M. Attallah, The influence of the laser scan strategy on grain structure and cracking behaviour in SLM powder-bed fabricated nickel superalloy, J. Alloys Compd. 615 (2014) 338–347. doi:10.1016/j.jallcom.2014.06.172.

[6] J. Jones, M. Whittaker, R. Buckingham, R. Johnston, M. Bache, D. Clark, Microstructural characterisation of a nickel alloy processed via blown powder direct laser deposition (DLD), Mater. Des. 117 (2017) 47–57. doi:10.1016/j.matdes.2016.12.062.

[7] L.N. Carter, X. Wang, N. Read, R. Khan, M. Aristizabal, K. Essa, M.M. Attallah, Process optimisation of selective laser melting using energy density model for nickel based superalloys, Mater. Sci. Technol. 0 (2015) 1743284715Y.000. doi:10.1179/1743284715Y.0000000108.

[8] R.J. Moat, a. J. Pinkerton, L. Li, P.J. Withers, M. Preuss, Residual stresses in laser direct metal deposited Waspaloy, Mater. Sci. Eng. A. 528 (2011) 2288–2298. doi:10.1016/j.msea.2010.12.010.

[9] M.M. Attallah, R. Jennings, X. Wang, L.N. Carter, Additive manufacturing of Ni-based superalloys: The outstanding issues, MRS Bull. 41 (2016) 758–764. doi:10.1557/mrs.2016.211.

[10] R.J. Moat, M. Karadge, A.J. Pinkerton, A. Deschamps, F. Bley, L. Li, P.J. Withers, M. Preuss, Intragranular precipitation variations in laser deposited Waspaloy due to compositional inhomogeneities, in: TMS Annu. Meet., 2007.

[11] T. Etter, K. Kunze, F. Geiger, H. Meidani, Reduction in mechanical anisotropy through high temperature heat treatment of Hastelloy X processed by Selective Laser Melting (SLM), IOP Conf. Ser. Mater. Sci. Eng. 82 (2015) 12097. doi:10.1088/1757-899X/82/1/012097.

[12] T. Trosch, J. Strößner, R. Völkl, U. Glatzel, Microstructure and mechanical properties of selective laser melted Inconel 718 compared to forging and casting, Mater. Lett. 164 (2016) 428–431. doi:10.1016/j.matlet.2015.10.136.

[13] R. Muñoz-Moreno, V.D. Divya, S.L. Driver, O.M.D.M. Messé, T. Illston, S. Baker, M.A. Carpenter, H.J. Stone, Effect of heat treatment on the microstructure, texture and elastic anisotropy of the nickel-based superalloy CM247LC processed by selective laser melting, Mater. Sci. Eng. A. 674 (2016) 529–539. doi:10.1016/j.msea.2016.06.075.

[14] S. Li, H. Xiao, K. Liu, W. Xiao, Y. Li, X. Han, J. Mazumder, L. Song, Melt-pool motion, temperature variation and dendritic morphology of Inconel 718 during pulsed- and continuous-wave laser additive manufacturing: A comparative study, Mater. Des. 119 (2017) 351–360. doi:10.1016/j.matdes.2017.01.065.

[15] D. Clark, S.D. Sharples, D.C. Wright, Development of online inspection for additive manufacturing products, Insight Non-Destructive Test. Cond. Monit. 53 (2011) 610–613. doi:10.1784/insi.2011.53.11.610.

[16] F. Geiger, K. Kunze, T. Etter, Tailoring the texture of IN738LC processed by selective laser melting (SLM) by specific scanning strategies, Mater. Sci. Eng. A. 661 (2016) 240–246. doi:10.1016/j.msea.2016.03.036.

[17] LaVision, StrainMaster8.3, Goettingen, 2016.

[18] H. Schreier, J.J. Orteu, M.A. Sutton, Image correlation for shape, motion and deformation measurements: Basic concepts, theory and applications, 2009. doi:10.1007/978-0-387-78747-3.

[19] D. Dye, H.J. Stone, R.C. Reed, A two phase elastic-plastic self-consistent model for the accumulation of microstrains in Waspaloy, Acta Mater. 49 (2001) 1271–1283. doi:10.1016/S1359-6454(01)00003-9.

[20] F. Di Gioacchino, J. Quinta da Fonseca, Plastic Strain Mapping with Sub-micron Resolution Using Digital Image Correlation, Exp. Mech. 53 (2013) 743–754. doi:10.1007/s11340-012-9685-2.

[21] Y.B. Das, A.N. Forsey, T.H. Simm, K.M. Perkins, M.E. Fitzpatrick, S. Gungor, R.J. Moat, In situ observation of strain and phase transformation in plastically deformed 301 austenitic stainless steel, Mater. Des. 112 (2016). doi:10.1016/j.matdes.2016.09.057.

[22] W. Clocksin, A New Method for Computing Optical Flow, Procedings Br. Mach. Vis. Conf. 2000. (2000) 13.1-13.10. doi:10.5244/C.14.13.

[23] V.D. Divya, R. Muñoz-Moreno, O.M.D.M. Messé, J.S. Barnard, S. Baker, T. Illston, H.J. Stone, Microstructure of selective laser melted CM247LC nickel-based superalloy and its evolution through heat treatment, Mater. Charact. 114 (2016) 62–74. doi:10.1016/j.matchar.2016.02.004.